Front. Chem. Sci. Eng. 2023, 17(4): 449–459
https://doi.org/10.1007/s11705-022-2226-3

RESEARCH ARTICLE

Construction of defect-containing UiO-66/$MoSe_2$ heterojunctions with superior photocatalytic performance for wastewater treatment and mechanism insight

Xiao Han[1,2], Xiaoxuan Wang[1,2], Jiafang Wang[1,2], Yingjie Xie[1,2], Cuiwei Du[1,2], Chongfei Yu[1,2], Jinglan Feng[1,2], Jianhui Sun (✉)[1,2], Shuying Dong (✉)[1,2]

1 School of Environment, Henan Normal University, Xinxiang 453007, China
2 Key Laboratory for Yellow River and Huai River Water Environmental and Pollution Control, Ministry of Education, Xinxiang 453007, China

Abstract Metal–organic frameworks are recognized as promising multifunctional materials, especially metal–organic framework-based photocatalysts, which are considered to be ideal photocatalytic materials. Herein, a new type of UiO-66/$MoSe_2$ composite was prepared using the solvothermal method. The optimum composite was selected by adjusting the mass ratio of UiO-66 and $MoSe_2$. X-ray diffraction analysis showed that the mass ratio influenced the crystal plane exposure rate of the composite, which may have affected its photocatalytic performance. The composite is composed of ultra-thin flower-like $MoSe_2$ that wrapped around cubic UiO-66, a structure that increases the abundance of active sites for reactions and is more conducive to the separation of carriers. The photocatalytic properties of the composite were evaluated by measuring the degradation rate of Rhodamine B and the catalyst's ability to reduce Cr(VI)-containing wastewater under visible light irradiation. Rhodamine B was decolorized completely in 120 min, and most of the Cr(VI) was reduced within 150 min. The photochemical mechanism of the complex was studied in detail. The existence of Mo^{6+} and oxygen vacancies, in addition to the Z-type heterojunction promote the separation of electrons and holes, which enhances the photocatalytic effect.

Keywords UiO-66/$MoSe_2$, photocatalysis, dye-containing wastewater, heavy metal wastewater, oxygen vacancies

Received June 5, 2022; accepted July 26, 2022

E-mails: sunjhhj@163.com (Sun J.),
shidashuying@163.com (Dong S.)

1 Introduction

Environmental pollution is a major issue worldwide, making it imperative to develop sustainable energy technology [1]. In particular, water pollution is a major problem in most countries. For example, dye wastewater and heavy metal wastewater severely affect human health [2–4]. This type of wastewater is especially toxic and difficult to treat with traditional wastewater treatment methods, possibly leading to secondary pollution. Photocatalysis has been developed as a new type of energy-saving wastewater treatment technology that does not generate secondary pollution [5,6]. However, there are certain challenges when facing the use of photocatalytic materials, such as poor light utilization. Developing a new type of material to solve environmental and energy issues is a major focus of current research [7,8].

Metal–organic frameworks (MOFs) are multifunctional materials developed in recent years, and are used in gas adsorption [9], drug transport [10], sensors [11] and catalysis technology [12]. MOFs have the advantages of a high specific surface area, porous properties, and adjustability, making them an ideal photocatalyst [13,14]. MOFs play a dominant role in conventional semiconductor photocatalysts due to the combination of metal-oxygen clusters and bridging organic linkers, providing highly crystalline porous structures with large surface areas. Metal clusters in MOF act as quantum dots for light collection, while organic linkers act as antennas to enhance the absorption of electromagnetic radiation [15]. As an important type of MOF, UiO-66(Zr) materials are expected to be the most promising MOF materials for practical applications owing to their outstanding stability

and functional applications [16–18]. Unfortunately, the photocatalytic performance of UiO-66(Zr) is not ideal due to limited light absorption. To improve its photocatalytic activity, UiO-66(Zr) is usually doped with noble metals or combined with other semiconductor materials. For example, Liu et al. [19] developed flower-like $ZnIn_2S_4$/UiO-66 microspheres by a hydrothermal method, which could reduce Cr(VI) in wastewater by 99% within 60 min. Sha et al. [20] prepared an Ag_2CO_3/UiO-66 composite with excellent photocatalytic performance for the degradation of Rhodamine B (RhB), and compared it to the physical mixture of the two materials. Cao et al. [21] doped Co into UiO-66, which broadened its light absorption properties and promoted electron transfer, greatly improving its tetracycline adsorption and photocatalytic performance. Therefore, UiO-66s has significant application prospects in the fields of catalysis and energy [22].

$MoSe_2$ has a honeycomb structure that is similar to that of graphene. $MoSe_2$ nanosheets have many active sites on their edges and a narrow band gap; therefore, they are excellent photocatalysts [23–26]. However, pure $MoSe_2$ easily agglomerates into large blocks during synthesis, which likely results in electron–hole recombination and poor cycle performance. Therefore, $MoSe_2$ is generally monolayered or composited with other materials for use in photocatalytic experiments. For instance, Wu et al. [27] prepared $MoSe_2$ nanoflower balls composed of single-layer sheets and few-layer sheets using a simple hydrothermal method, and analyzed their redox performance as piezoelectric catalysts. The $MoSe_2$ flower balls were able to use piezoelectric vibration to generate active oxygen groups, achieving the complete degradation of RhB dye within 120 s. Zhang et al. [28] used a colloidal chemical synthesis method to prepare 3D-structured $MoSe_2$ microspheres, which exhibited superior electrocatalytic hydrogen evolution performance. Wang et al. [29] prepared a C-fiber@$MoSe_2$ nanoplate core–shell composite that demonstrated greatly improved photocatalytic activity driven by solar energy because C-fibers promote the transfer of photogenerated electrons.

Herein, we prepared UiO-66/$MoSe_2$ composites using a hydrothermal method. Ultra-thin $MoSe_2$ nanosheets were grown on the UiO-66 surface, which not only prevents the $MoSe_2$ from agglomerating into large blocks but also increases the specific surface area of the UiO-66 and the number of active sites available for the reaction. Furthermore, the thin $MoSe_2$ forms a 3D path for electron transfer, allowing the electrons and holes to achieve efficient separation. Then, the photocatalytic degradation of RhB-containing wastewater and Cr(VI)-containing wastewater was investigated. The prepared composite catalyst exhibited good photocatalytic performance and stability. This study provides a theoretical basis for the application of zirconium-MOF materials in water treatment.

2 Experimental

2.1 Preparation of UiO-66 catalyst

UiO-66 was prepared by the solvothermal method in *N*,*N*-dimethylformamide (DMF). 80.4 mg $ZrCl_4$ and 57.3 mg H_2BDC were dissolved in 40 mL DMF and the resultant solution was marked A. A was transferred to a stainless steel autoclave and held at 120 °C for 6 h. After the autoclave was cooled to room temperature, the precipitate was collected by centrifugation and washed with DMF and ethanol several times. Finally, the sample was dried to a constant weight in a vacuum drying oven.

2.2 Preparation of $MoSe_2$ catalyst

$MoSe_2$ was prepared by reducing Se with hydrazine hydrate under hydrothermal conditions. The specific experimental process was as follows: $Na_2MoO_4{\cdot}6H_2O$ (0.4839 g) was dissolved in 50 mL deionized water, and the solution was labeled X. Meanwhile, 0.2318 g Se was added into 10 mL hydrazine hydrate, after which the solution was dispersed by ultrasound for 1 h and labeled Y. Then, X and Y were evenly mixed and the mixture was transferred into a stainless steel autoclave and held at 180 °C for 24 h. After the autoclave had cooled to room temperature naturally, the precipitate was collected by centrifugation and washed with H_2O and ethanol several times, before drying to constant weight in a vacuum drying oven.

2.3 Preparation of UiO-66(Zr)/$MoSe_2$ catalyst

Various amounts of $MoSe_2$ (0.033, 0.05, 0.075, 0.1, and 0.125 g) were added to solution A (2.1), and the mixed solution was transferred to a stainless steel autoclave and held at 120 °C for 6 h (Scheme 1). After the autoclave cooled down to room temperature, the precipitate was collected by centrifugation and washed with DMF and ethanol several times. Finally, it was dried to constant weight in a vacuum drying oven. The prepared catalysts were marked as ZM-32, ZM-22, ZM-23, ZM-24, and ZM-25, according to the mass ratio of UiO-66 and $MoSe_2$ varying between 3:2 and 2:5. The mass of UiO-66 is

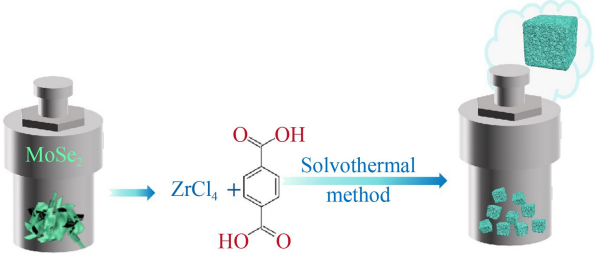

Scheme 1 Schematic illustrating the synthesis of UiO-66/$MoSe_2$.

taken as the average mass of the prepared UiO-66 from three parallel experiments.

2.4 Characterization

X-ray diffraction (XRD) was conducted using a Bruker-D8-AXS diffractometer (Bruker Co., Germany) which was configured with Cu Kα radiation (λ = 0.15406 Å). The 2θ collection range of the pattern was 5°–70°. Transmission electron microscopy (TEM) was conducted to observe the morphology of the samples using a JEM 2100 Electron Microscope (JEOL Ltd., Japan). Ultraviolet–visible diffuse reflectance spectroscopy (UV–vis DR) was performed using a UV–vis-NIR spectrophotometer (Lambda 950, PerkinElmer) with $BaSO_4$ as the reference and a spectral monitoring range of 300–800 nm. The elements and elemental states of the sample were analyzed by X-ray photoelectron spectroscopy (XPS) (Escalab-250), configured with Al Kα (150 W). The specific surface area (Brunauer–Emmett–Teller, BET) and pore structure of the samples were determined by the Belsorb-max Surface Area and Pore Size Analyzer (Microtrac BEL) at –196 °C. An electron spin resonance (ESR) spectrometer (Bruker, JES-FA200) was used to detect electron paramagnetic resonance and ESR signals in the 5,5-dimethyl-1-pyrroline N-oxide (DMPO) solution at room temperature.

The photocatalytic performance of the prepared photocatalysts was evaluated using simulated wastewater under simulated sunlight irradiation (500 W Xenon lamp). For each photocatalytic reaction, 25 mg of the catalyst was dispersed in 50 mL wastewater solution under magnetic stirring. Before the light source irradiation commenced, the suspension was adsorbed for 30 min to achieve an adsorption–desorption equilibrium between the catalysts and the pollutants (without light). The wastewater suspension solution (4 mL) was sampled every 30 min after irradiation, and the supernatant was collected for analysis. The concentration of pollutants was determined by measuring the absorbance of the supernatant at the relevant wavelength of maximum absorption for the pollutants using a UV–vis spectrophotometer (UV-1700, SHIMADZU). The calculation formula of the degradation efficiency is:

$$\text{Degradation efficiency}(100\%) = (1 - C_t/C_0) \times 100\%, \quad (1)$$

where C_0 is the concentration after adsorption–desorption equilibrium, and C_t is the concentration in wastewater at reaction time t (h).

In addition, the photocatalytic reduction performance of the prepared samples was determined by measuring the reduction of Cr(VI) in wastewater. The equipment and experimental method used were consistent with the aforementioned photocatalytic reaction. The Cr(VI) concentration was determined by diphenylcarbazide spectrophotometry in the wastewater. Specifically, 1 mL of the centrifuged supernatant was added to a 50 mL colorimetric tube and diluted up to the mark with water. Then, 0.5 mL of H_2SO_4 (1 + 1) and 0.5 mL of H_3PO_4 (1 + 1) were added, the mixture was shaken, and 2 mL of diphenylcarbazide solution was added. The absorbance of the mixture was measured at a wavelength of 540 nm after shaking for 5–10 min. The degradation efficiency of Cr(VI) was calculated using formula (1).

2.5 Electrochemical activity tests

The photoelectric properties of the samples were tested using an electrochemical workstation (Zahner Zennium, Germany), which employed a traditional three-electrode system. The reference electrode and the counter electrode were Ag/AgCl and a Pt sheet, respectively, while Na_2SO_4 solution (0.5 mol·L^{-1}) was used as the electrolyte. The working electrode was prepared as follows: 0.03 g of catalyst was dispersed in 2 mL of ethanol under ultrasonic conditions, and the suspension was dropped onto a fluorine-doped tin oxide substrate, and dried to form a 1 cm × 1 cm film. The light response was measured by recording the photocurrent under irradiation with a 300 W xenon lamp. Electrochemical impedance spectroscopy (EIS) was performed from 0.01 to 100 kHz using the potentiostatic method (5 mV).

3 Results and discussion

Figure 1 shows the XRD patterns of the prepared samples. As shown in Fig. 1(a), the shape and position of the diffraction peaks were completely consistent with those for the UiO-66 reported in the literature, demonstrating that the prepared sample was indeed UiO-66, as expected; its peaks were located at 2θ = 7.35°, 8.58°, 12.02°, and 25.68° [30]. Figure 1(b) shows the XRD spectrum of $MoSe_2$, whose crystal form and phase conformed to the characteristic peak of $MoSe_2$ (JCPDS No. 29-0914). The peaks located at 32.15°, 35.14° and 55.61° correspond to the crystal planes of (100), (102) and (110) of $MoSe_2$, respectively. Figure 1(c) is the XRD pattern of the prepared composites. Due to the high intensities of the characteristic peaks of UiO-66, the crystalline form of $MoSe_2$ could not be observed in the composites when the mass ratio of UiO-66 and $MoSe_2$ was less than 2:3. It could be seen that the diffraction peak intensity for UiO-66 became weaker with increasing $MoSe_2$ ratios, while the peak belonging to $MoSe_2$ gradually appeared (Fig. 1(d)). These results indicated that the addition of excessive $MoSe_2$ negatively affects the crystallinity of UiO-66.

Figure 2 shows the images of the prepared samples. The prepared UiO-66 particles approximated to relatively regular cubes, with a particle size of about 80 nm (Fig. 2(a)), while the prepared $MoSe_2$ had a thin layer

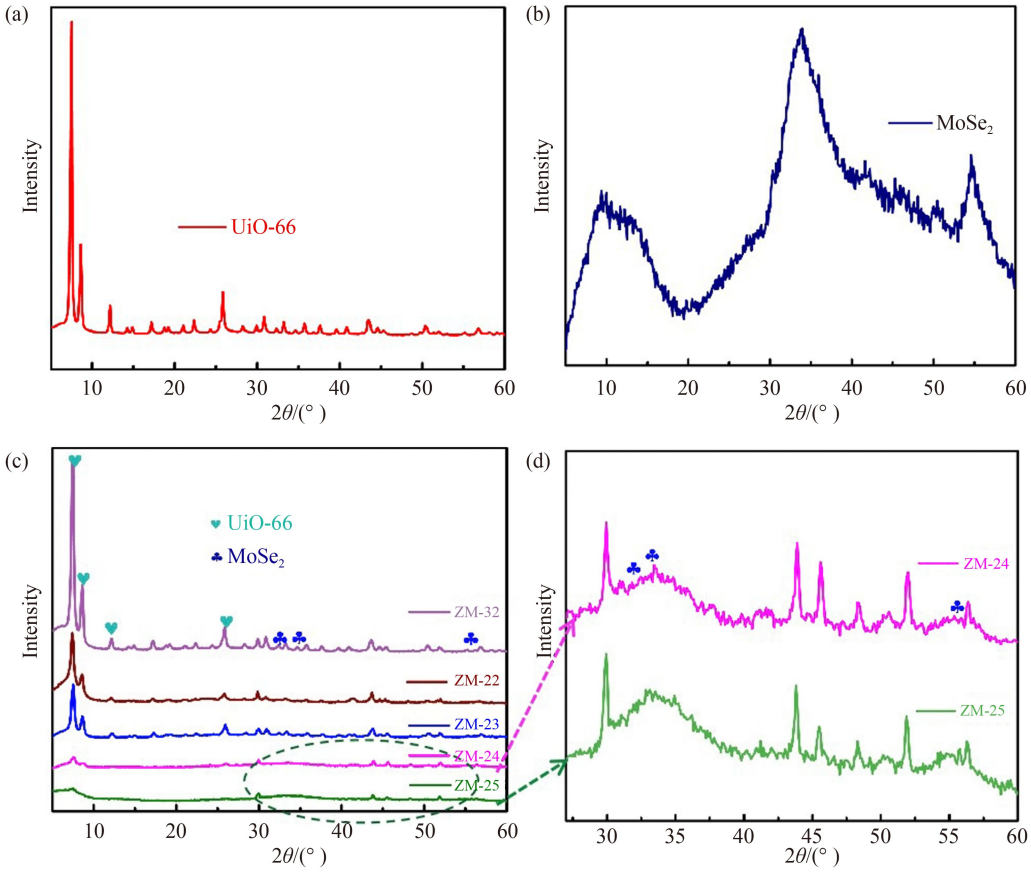

Fig. 1 XRD patterns of (a) UiO-66, (b) $MoSe_2$, (c) composites, and (d) detail patterns of ZM-24 and ZM-25.

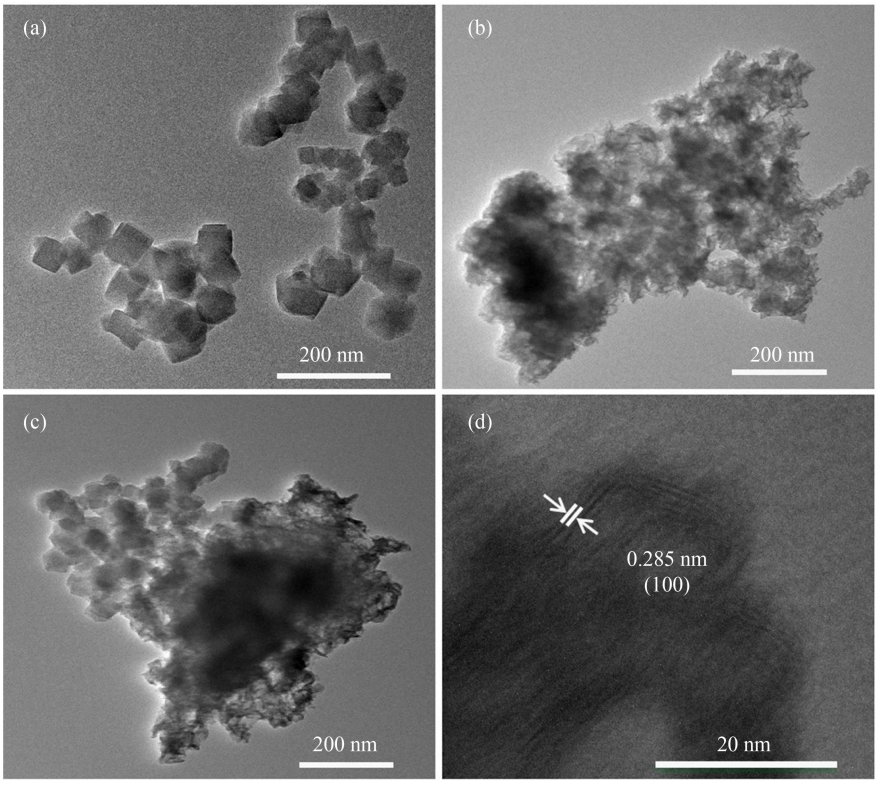

Fig. 2 TEM micrographs of (a) UiO-66, (b) $MoSe_2$, (c) ZM-23, and (d) the lattice fringes of ZM-23.

structure stacked into flowers (Fig. 2(b)). Figure 2(c) shows the TEM image of the composite, where part of the UiO-66 could be observed to be wrapped up in a layered sheet of $MoSe_2$, increasing the abundance of active sites for the reaction. The lattice fringes of ZM-23 in Fig. 2(d) correspond to the (100) crystal plane of $MoSe_2$.

The photocatalytic performance of the prepared samples was influenced by their light absorption performance (Fig. 3). Figure 3(a) shows the UV–vis light absorption performance of the prepared samples. UiO-66 exhibited a strong absorption peak in the UV region; however, it had almost no absorption in the visible region. In contrast, $MoSe_2$ demonstrated excellent absorption in the visible region, which attributed to the black color of the material. In comparison to UiO-66, the composite absorbed more light in the visible range, and the edge of the absorption band was red-shifted. It is well known that the band gap energy of semiconductors can be calculated from the UV–vis DR spectra, according to Eq. (2),

$$Ah\nu = C(h\upsilon - E_g)^{1/2}, \quad (2)$$

where A and υ represent the absorption coefficient and radiation frequency, respectively, which can be calculated from Fig. 3(a). h and C represent the Planck constant and a constant, respectively. The E_g (band-gap energy) can be estimated from Fig. 3(b). The E_g of UiO-66 was 3.7 eV, while the E_g of $MoSe_2$ was 1.53 eV [31]. The results correspond to Fig. 3(a) and demonstrate that $MoSe_2$ exhibits a superior response to visible light.

XPS was conducted to determine the elements and their states in the samples (Fig. 4). Figure 4(a) shows the high-resolution full spectrum of the prepared catalyst. Figure 4(b) shows the high-resolution spectra of Zr 3d in UiO-66 and ZM-23. UiO-66 exhibited two peaks at 184.75 and 182.35 eV, which were attributed to the presence of Zr in the Zr–O cluster [19]. In comparison to UiO-66, the characteristic peaks of Zr in ZM-23 shifted to a higher binding energy, indicating an interaction between UiO-66 and $MoSe_2$. There were three main peaks for C 1s (Fig. 4(c)), located at 284.7, 285.4, and 288.8 eV, which were attributed to the C sp^2 in the benzene ring, C–O, and O–C–O [32], respectively. The center portion of the peaks at the center of 228.6 and 231.4 eV represented Mo^{4+} (Figs. 4(e) and 4(f)) [33–35], while the additional peaks in sample ZM-23 at 232.7 and 235.8 eV represented Mo^{6+} [36,37]. Mo^{6+} was formed by oxidation due to the higher activity of the Mo edge in $MoSe_2$ during the hydrothermal process [36]. The defect formation of Mo^{6+} had a certain influence on the photocatalytic reactions. Finally, the peaks for Se 3d represented Se^{2+} in $MoSe_2$ (Fig. 4(d)) [31,38]. In comparison to $MoSe_2$, the characteristic peaks of Mo and Se in ZM-23 shifted to a lower binding energy, indicating that photogenerated electrons transferred from UiO-66 to $MoSe_2$. The band structure was determined from the XPS spectrum (Fig. S1, cf. Electronic Supplementary Material, ESM), and which demonstrates that the valence band position/the highest occupied molecular orbital (HOMO) potential of $MoSe_2$ and UiO-66 were 0.366 and 3.61 eV, respectively.

Nitrogen adsorption–desorption isotherms reflect the pore structure and pore size of the prepared catalysts, as shown in Fig. 5. The nitrogen adsorption and desorption curves for UiO-66 and $MoSe_2$ were consistent with a type II isotherm (Brunauer–Deming–Deming–Teller-classification), which reflected typical physical adsorption processes on non-porous or macroporous adsorbents. However, the pore size distribution in Fig. 5(b) suggests that the prepared material is a macroporous material. It should be noted that the N_2 adsorption−desorption curve of the composite was completely different from that of the pure material, as it exhibited a type IV isotherm (Brunauer–Deming–Deming–Teller classification) with an H1 hysteresis loop, indicating that the material was a typical mesoporous material. This phenomenon further indicates that there was a special interaction between $MoSe_2$ and UiO-66. Table 1 shows the BET surface area,

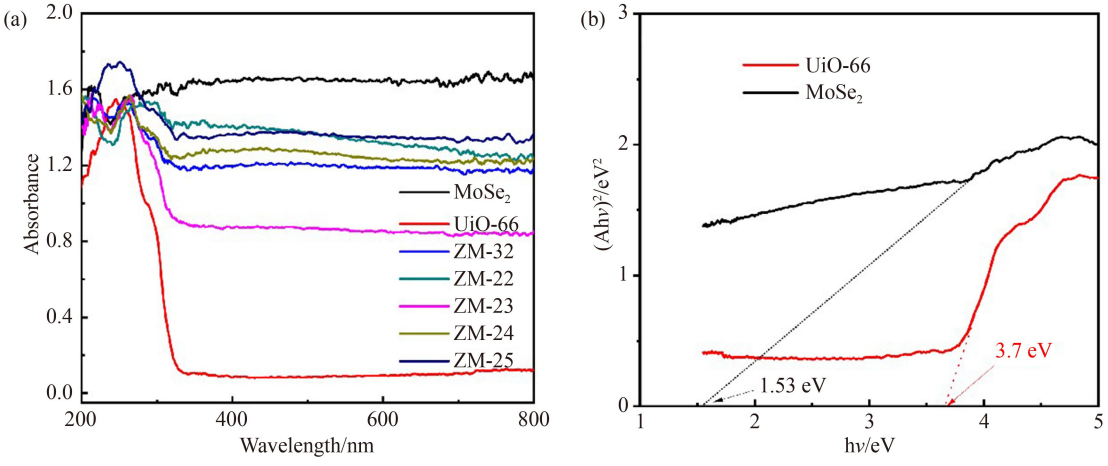

Fig. 3 (a) UV–vis diffuse reflectance spectra and the relationship between $(Ah\nu)^{1/2}$ and (b) the photon energy hν of UiO-66 and $MoSe_2$.

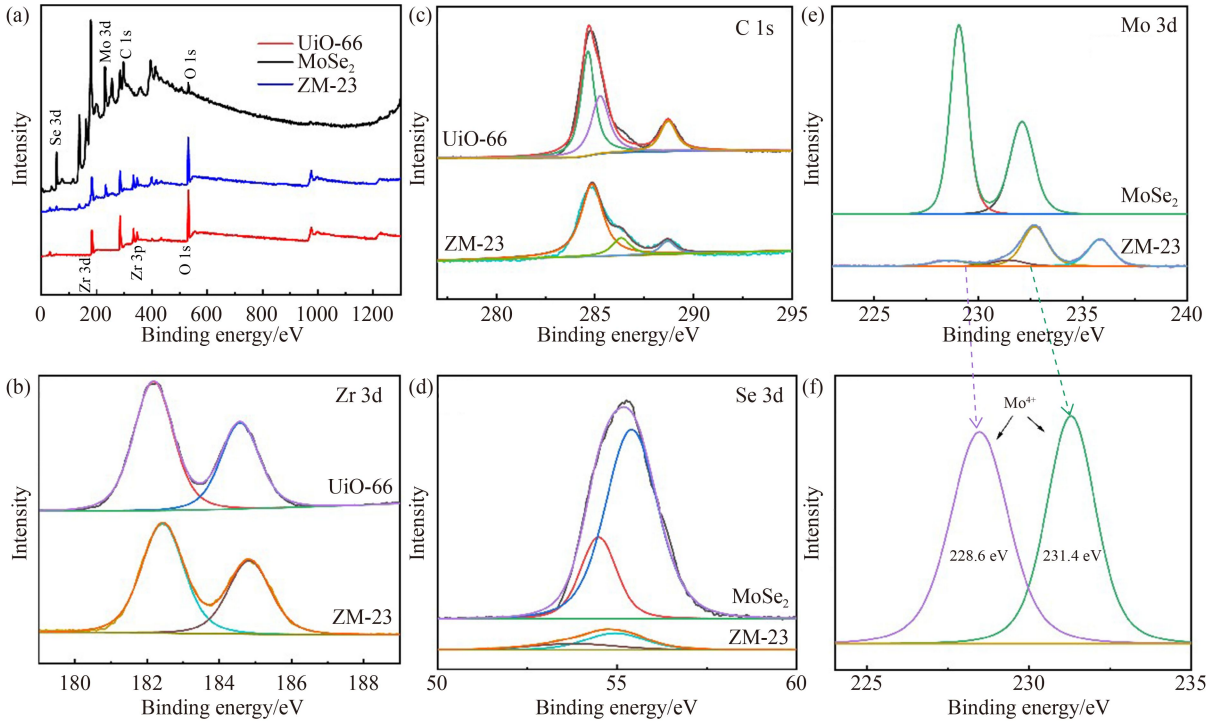

Fig. 4 Full spectrum of (a) the prepared catalyst, and high-resolution XPS spectra of (b) Zr 3d, (c) C 1s, (d) Se 3d, (e, f) Mo 3d.

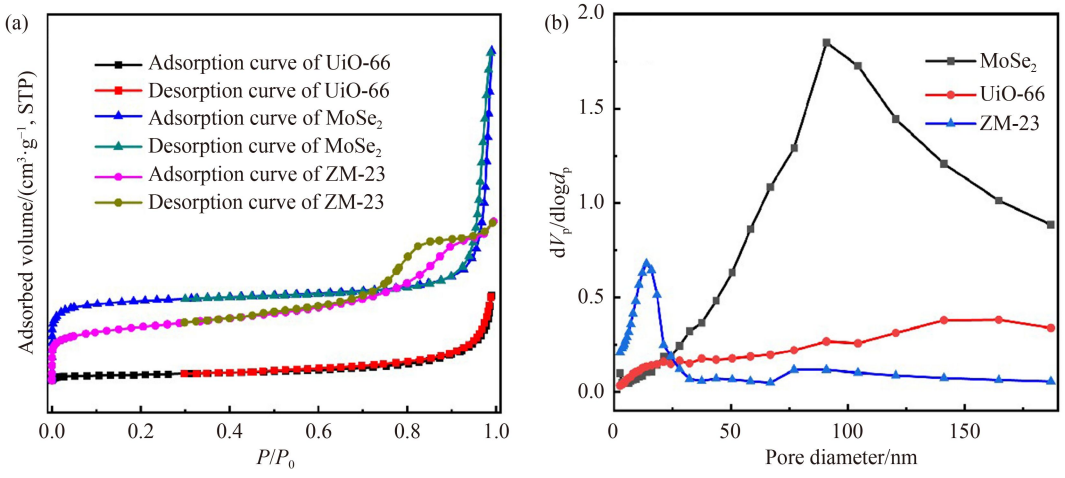

Fig. 5 (a) Nitrogen adsorption–desorption isotherms and (b) the corresponding pore size distribution curves of the as-synthesized UiO-66, $MoSe_2$ and ZM-23 photocatalysts.

pore volume, and pore diameter of the prepared samples. The BET surface area of UiO-66 (700.65 $m^2 \cdot g^{-1}$) was much larger compared to than those of the other catalysts.

The separation efficiency of electrons and holes directly affects the photocatalytic activity of the catalyst, and electrochemical measurements can be used to the study electron transfer (Fig. 6) [39,40]. Figure 6(a) shows the EIS diagram of the prepared samples, where the semicircle represents the diameter of the Nyquist circle. Smaller diameters lead to faster interfacial charge transfer. The results show that ZM-23 had a faster charge transfer rate, which could lead to higher electron separation efficiency, in comparison to the other catalysts.

Table 1 Comparison of the nitrogen adsorption characteristics of UiO-66, $MoSe_2$, and ZM-23

Sample	BET surface area[a)]/($m^2 \cdot g^{-1}$)	Pore volume[b)]/($cm^3 \cdot g^{-1}$)	Pore diameter[c)]/nm
UiO-66	700.65	1.182	6.7487
$MoSe_2$	47.939	0.302	25.203
ZM-23	378.67	0.3976	4.2

Figure 6(b) showed the photocurrent tests of UiO-66, $MoSe_2$, and ZM-23 under xenon lamp irradiation. The photocurrent response of UiO-66 was very small, while the current density of ZM-23 was the highest under the same conditions, indicating that the electron–hole

separation efficiency was the highest for ZM-23.

Figure S2 (cf. ESM) is a diagram of the dark adsorption of the prepared materials. At 30 min, the individual materials reached adsorption saturation, therefore, the dark adsorption time was set to 30 min before photocatalysis. The properties of the prepared catalysts were shown in Fig. 7. The degradation efficiencies of RhB by prepared photocatalysts under simulated sunlight irradiation are shown in Fig. 7(a). The composite materials had higher photocatalytic activity than pure UiO-66 and $MoSe_2$. With increasing of Zr/Mo in the composite materials, their photocatalytic activity first increased and then exhibited a decreasing trend, ZM-23 had the best photocatalytic activity, with RhB (10 mg·L^{-1}) being completely decolorized in 120 min. Figure 7(b) shows the kinetic constants of each catalyst in the degradation of wastewater, and the kinetic constant of ZM-23 was as high as 0.03342, which is 10 times that of pure UiO-66 and 4 times that of pure $MoSe_2$.

The photocatalytic reduction performance of the prepared materials was evaluated by testing their ability to a reduce Cr(VI) solution under simulated sunlight irradiation (Fig. 8). It can be seen from Fig. 8(a) that the prepared catalysts were able to measurably reduce Cr(VI) in a certain concentration of Cr(VI) solution. Among them, UiO-66 had the weakest ability to reduce Cr(VI), while the photocatalytic reduction performance of ZM-23 was better than those of other materials. Moreover, an analysis of the reaction kinetics showed that the reduction of Cr(VI) was in accordance with first-order kinetics. By calculating its kinetic constant, the constant for ZM-23 was found to be larger than those of the other materials.

The recycling performance of the photocatalyst is also an important factor to evaluate its potential for industrial application. Figure 9 shows the results of a cycling experiment and a quenching experiment. Figure 9(a) showed the effects of recycling on the performance of the ZM-23 catalyst. After three cycles, the photocatalytic performance of ZM-23 did not significantly decrease, demonstrating that the catalyst has good stability and cycle performance. Figure 9(b) displays the results of a quenching experiment to explore the active species in the photocatalytic reaction. In this experiment, ethylenediamine tetraacetic acid (EDTA), methanol (MeOH), and

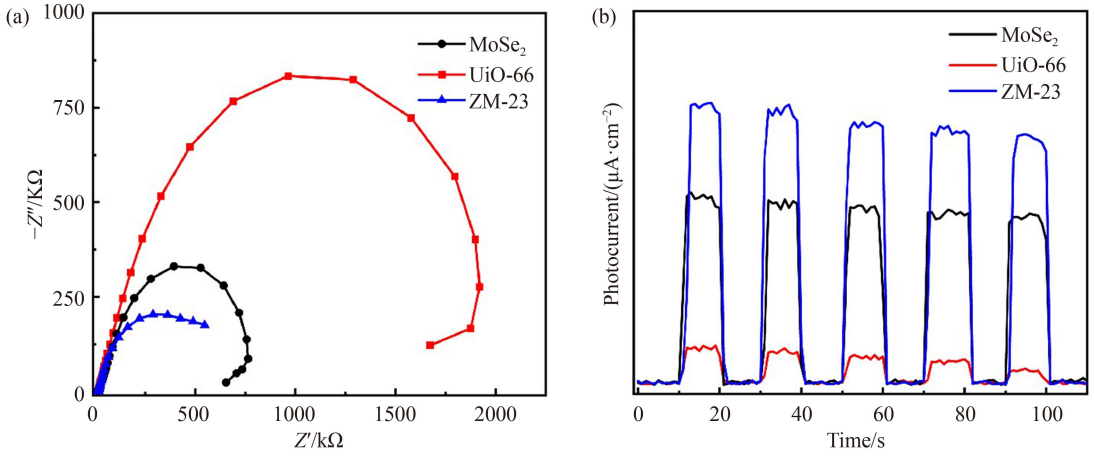

Fig. 6 (a) Nyquist plots of the electrochemical impedance spectra and (b) photocurrent response of UiO-66, $MoSe_2$ and ZM-23 photocatalysts.

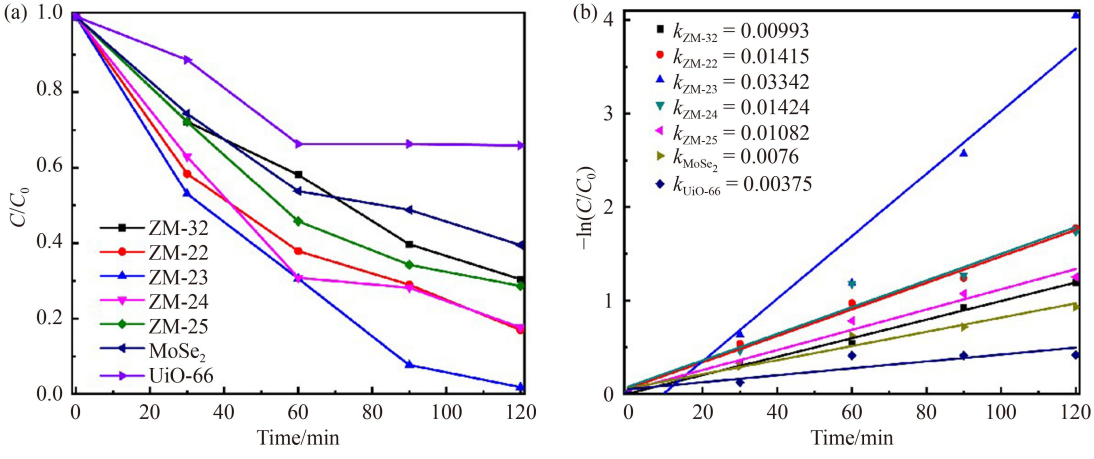

Fig. 7 (a) Degradation efficiencies of RhB by prepared photocatalysts under simulated sunlight irradiation and (b) $\ln(C_0/C)$ versus time for RhB under simulated sunlight irradiation.

isopropanol (IPA) were used as quenchers to capture photogenerated holes (h^+), superoxide radicals ($\cdot O_2^-$), and hydroxyl radicals ($\cdot OH$), respectively. In comparison to the blank group (which lacked a quencher), the addition of MeOH had the greatest impact on the photocatalytic performance, followed by the addition of EDTA, which had some impact on performance, while the addition of IPA had the least effect on the photocatalysis. The results reveal that the free radicals that play the greatest role in the photocatalytic reaction are h^+ and $\cdot O_2^-$ radicals.

To further confirm the active species involved in the reaction, ESR spin-trapping used DMPO as the capturing agent was performed to measure the h^+ and $\cdot O_2^-$ radicals in the photocatalytic reaction (Fig. 10). The needle signal in Fig. 10(a) indicates the presence of h^+, and a stronger signal indicates excess trapping agent and lower h^+. Figure 10(b) shows the signal diagrams for $\cdot O_2^-$ radicals. No signals were observed for $\cdot O_2^-$ radicals under dark conditions; however, when exposed to visible light for 10 min, a four-wire signal for $\cdot O_2^-$ radicals appeared, indicating that the $\cdot O_2^-$ radicals played a certain role in the reaction. This conclusion was consistent with the results of the capture experiment. Additionally, ESR was used to confirm the presence of oxygen vacancies in the composites (Fig. S3, cf. ESM). UiO-66 had no ESR signal belonging to oxygen vacancies, but ZM-23 had a strong signal, with a value of 2.003, indicating that there are abundant oxygen vacancies in ZM-23. The existence of oxygen vacancies may have a positive effect on the performance of the catalysts.

Based on the above research, two possible mechanisms for the photocatalytic activity of the prepared catalyst are discussed. The first possible photocatalytic mechanism is that UiO-66 and $MoSe_2$ form a traditional type II heterojunction (Scheme 2). The electrons in the valence band of $MoSe_2$ are excited to the conduction band, while the electrons in the HOMO potential of UiO-66 are excited to the lowest unoccupied molecular orbital (LUMO) potential. The holes in the HOMO potential of the UiO-66 catalyst transfer to the valence band of $MoSe_2$, and at the same time, the electrons in the conduction band of $MoSe_2$ are transferred to the HOMO

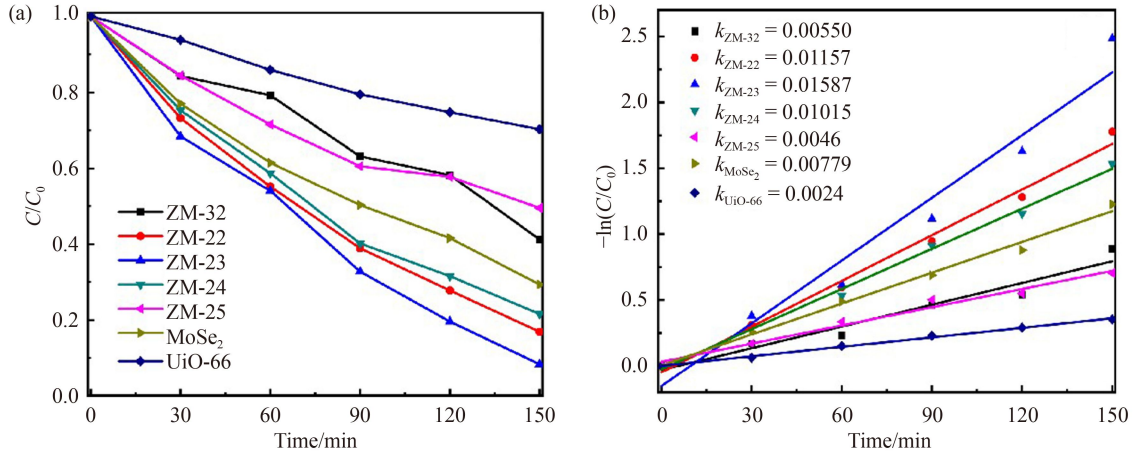

Fig. 8 (a) Reduction performance for a Cr(VI) solution under simulated sunlight irradiation and (b) $\ln(C_0/C)$ versus time for Cr(VI) under simulated sunlight irradiation.

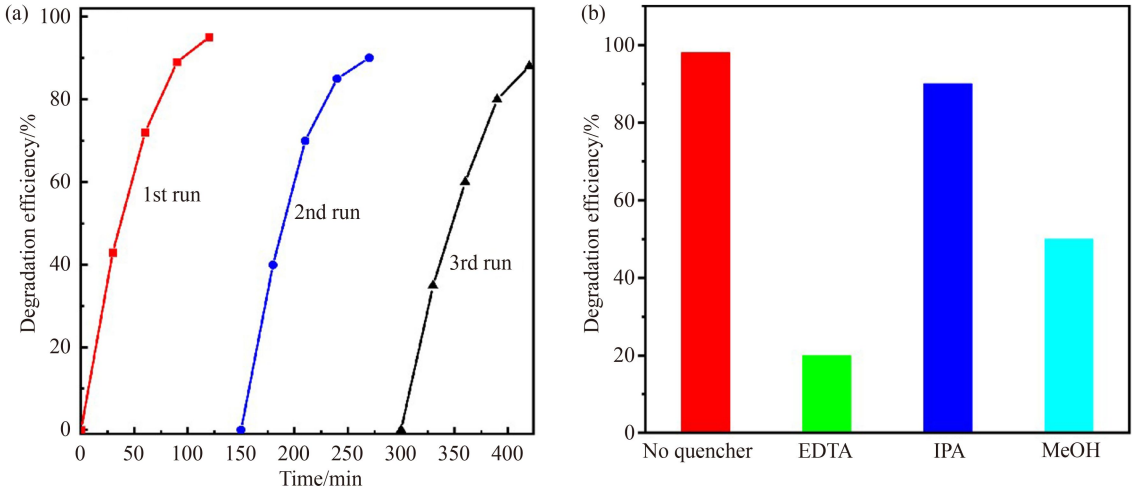

Fig. 9 (a) Cyclic degradation of RhB using ZM-23 and (b) the photocatalytic degradation of an RhB solution using ZM-23 with and without quenchers under simulated sunlight irradiation.

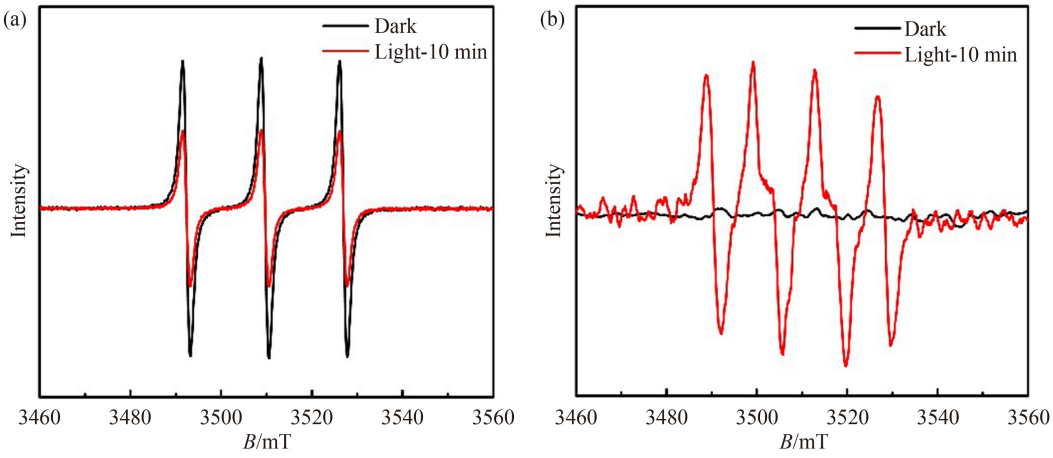

Fig. 10 ESR spin-trapping (a) h^+ and (b) $\cdot O_2^-$ radicals.

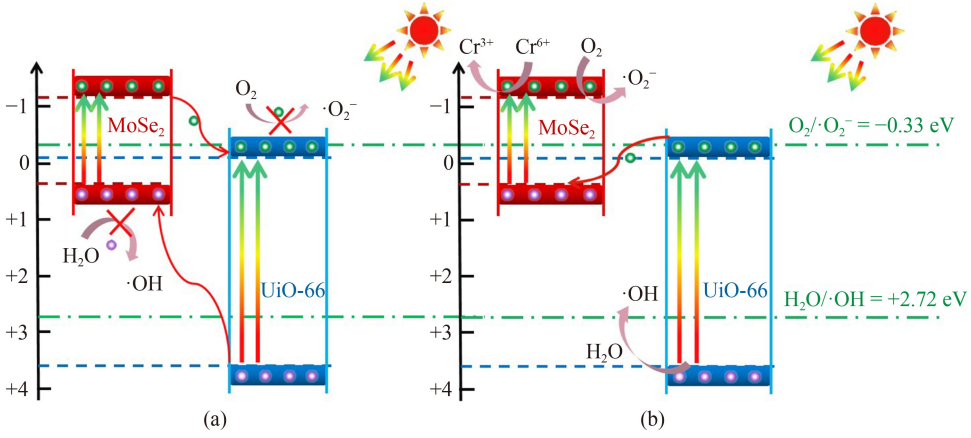

Scheme 2 Photocatalytic mechanism of (a) UiO-66 and $MoSe_2$ forming a traditional type II heterojunction and (b) Z-scheme heterojunction.

potential of UiO-66. However, because the valence band of $MoSe_2$ has a more negative redox potential than $E^{\theta}(H_2O/\cdot OH)$, the h^+ transfers to the $MoSe_2$ valence band could not reacted with water to form ·OH. Further, the electrons transferred to the UiO-66 conduction band also could not reacted with O_2 to form $\cdot O_2^-$ radicals to degrade pollutants. The active groups generated by this path rae limited, and photocatalytic degradation of pollutants cannot occur efficiently, therefore, the assumed traditional heterojunction theory is disproved.

$$\text{UiO-66} + h\nu \rightarrow e_{CB}^- + h_{VB}^+ \quad (3)$$

$$MoSe_2 + h\nu \rightarrow e_{CB}^- + h_{VB}^+ \quad (4)$$

$$h_{VB}^+(\text{UiO-66}) \rightarrow h_{VB}^+(MoSe_2) < E^{\theta}(H_2O/\cdot OH) = 2.72\ \text{eV vs. NHE} \quad (5)$$

$$e_{CB}^-(MoSe_2) \rightarrow e_{CB}^-(\text{UiO-66}) > E^{\theta}(O_2/\cdot O_2^-) = -0.33\ \text{eV vs. NHE} \quad (6)$$

Therefore, the reaction process is assumed to be a Z-scheme heterojunction (Scheme 2), After light irradiation excites the catalyst to generate electron and hole pairs, the electrons located in the LUMO potential of UiO-66 transfer to the valence state of $MoSe_2$ and recombine with the holes left behind, which is consistent with the XPS results. The holes in the HOMO potential of UiO-66 could react with H_2O to produce ·OH, which could further react with pollutants. Furthermore, the electrons in the conduction band of $MoSe_2$ can combine with the O_2 adsorbed on the surface to form $\cdot O_2^-$ radicals, which in turn oxidize the pollutants to CO_2 and H_2O.

$$e_{CB}^-(\text{UiO-66}) \rightarrow h_{VB}^+(MoSe_2) \quad (7)$$

$$h_{VB}^+(\text{UiO-66}) + H_2O \rightarrow \cdot OH \quad (8)$$

$$e_{CB}^-(MoSe_2) + \cdot O_2 \rightarrow \cdot O_2^- \quad (9)$$

$$\cdot O_2^-/OH + \text{pollutant} \rightarrow \text{small molecules} \rightarrow CO_2 + H_2O \quad (10)$$

4 Conclusions

In conclusion, we prepared cubic UiO-66 using a hydrothermal method and grew flower-like $MoSe_2$ on its surface. This composite exhibited excellent photocatalytic

activity due to the synergistic effect of these materials. The photocatalytic performance of the composite was evaluated according to the degradation of RhB-containing wastewater and the reduction of Cr(VI)-containing wastewater under simulated sunlight. RhB-containing wastewater was completely decolorized within 120 min and most of the Cr(VI) could be reduced within 150 min. In comparison to the two pure catalysts, the composite exhibited significantly improved photocatalytic degradation of RhB-containing wastewater and reduction of Cr(VI). The relevant electron transport and reaction mechanism were discussed. UiO-66(Zr) and $MoSe_2$ form a Z-type heterojunction, which facilitates for the effective separation of holes and electrons. Through various measurements, it was found that the composite species have Mo^{6+} and oxygen vacancy defects that positively impact photocatalysis in the heterojunction. This study provides a research basis for future scientific analyses in the field of MOFs-based photocatalysts.

Acknowledgements This work was supported by the National Natural Science Foundation of China (Grants Nos. 22076039, and 22176051), Natural Science Foundation of Henan Province (Grant No. 222300420054) and excellent Science and Technology Innovation Team of Henan Normal University (Grant No. 2021TD03).

Electronic Supplementary Material Supplementary material is available in the online version of this article at https://dx.doi.org/10.1007/s11705-022-2226-3 and is accessible for authorized users.

References

1. Wu Y, Li C, Tian Z, Sun J. Solar-driven integrated energy systems: state of the art and challenges. Journal of Power Sources, 2020, 478(2): 28762
2. Park E J, Jo H J, Kim H J, Cho K, Jung J. Effects of gamma-ray treatment on wastewater toxicity from a rubber products factory. Journal of Radioanalytical and Nuclear Chemistry, 2008, 277(3): 619–624
3. Landry K A, Boyer T H. Diclofenac removal in urine using strong-base anion exchange polymer resins. Water Research, 2013, 47(17): 6432–6444
4. Xiang Q, Yu J, Jaroniec M. Graphene-based semiconductor photocatalysts. Chemical Society Reviews, 2012, 41(2): 782–796
5. Dong S, Zhao Y, Yang J, Liu X, Li W, Zhang L, Wu Y, Sun J, Feng J, Zhu Y. Visible-light responsive PDI/rGO composite film for the photothermal catalytic degradation of antibiotic wastewater and interfacial water evaporation. Applied Catalysis B: Environmental, 2021, 291: 120127
6. Dong S, Zhao Y, Yang J, Li W, Luo W, Li S, Liu X, Guo H, Yu C, Sun J, Feng J, Zhu Y. Solar water recycling of carbonaceous aerogel in open and colsed systems for seawater desalination and wastewater purification. Chemical Engineering Journal, 2022, 431: 133824
7. Jian S, Tian Z, Hu J, Zhang K, Zhang L, Duan G, Yang W, Jiang S. Enhanced visible light photocatalytic efficiency of La-doped ZnO nanofibers via electrospinning-calcination technology. Advanced Powder Materials, 2022, 1(2): 100004
8. Dong S, Liu X, Tian G, Wang Y, Jin G, Zhao Y, Sun J, Fan M. Surface oxygen vacancies modified Bi_2MoO_6 double-layer spheres: enhanced visible LED light photocatalytic activity for ciprofloxacin degradation. Journal of Alloys and Compounds, 2022, 892: 162217
9. Zhou T, Sang Y, Sun Y, Wu C, Wang X, Tang X, Zhang T, Wang H, Xie C, Zeng D. Gas adsorption at metal sites for enhancing gas sensing performance of ZnO@ZIF-71 nanorod arrays. Langmuir, 2019, 35(9): 3248–3255
10. Suresh K, Matzger A J. Enhanced drug delivery by dissolution of amorphous drug encapsulated in a water unstable metal–organic framework (MOF). Angewandte Chemie International Edition, 2019, 58(47): 16790–16794
11. Yan B. Photofunctional MOF-based hybrid materials for the chemical sensing of biomarkers. Journal of Materials Chemistry C: Materials for Optical and Electronic Devices, 2019, 7(27): 8155–8175
12. Guo J, Qin Y, Zhu Y, Zhang X, Long C, Zhao M, Tang Z. Metal–organic frameworks as catalytic selectivity regulators for organic transformations. Chemical Society Reviews, 2021, 50(9): 5366–5396
13. Li Z, Guo J, Wan Y, Qin Y, Zhao M. Combining metal–organic frameworks (MOFs) and covalent-organic frameworks (COFs): emerging opportunities for new materials and applications. Nano Research, 2022, 15(4): 3514–3532
14. Qin Y, Wan Y, Guo J, Zhao M. Two-dimensional metal–organic framework nanosheet composites: preparations and applications. Chinese Chemical Letters, 2022, 33(2): 693–702
15. Guo J, Wan Y, Zhu Y, Zhao M, Tang Z. Advanced photocatalysts based on metal nanoparticle/metal–organic framework composites. Nano Research, 2021, 14(7): 2037–2052
16. Wang S, Guan B Y, Lou X W. Rationally designed hierarchical N-doped carbon@$NiCo_2O_4$ double-shelled nanoboxes for enhanced visible light CO_2 reduction. Energy & Environmental Science, 2018, 11(2): 306–310
17. Wang C C, Du X D, Li J, Guo X X, Wang P, Zhang J. Photocatalytic Cr(VI) reduction in metal–organic frameworks: a mini-review. Applied Catalysis B: Environmental, 2016, 193: 198–216
18. Shen L, Wu W, Liang R, Lin R, Wu L. Highly dispersed palladium nanoparticles anchored on UiO-66(NH_2) metal–organic framework as a reusable and dual functional visible-light-driven photocatalyst. Nanoscale, 2013, 5(19): 9374–9382
19. Liu B, Liu X, Liu J, Feng C, Li Z, Li C, Gong Y, Pan L, Xu S, Sun C Q. Efficient charge separation between UiO-66 and $ZnIn_2S_4$ flowerlike 3D microspheres for photoelectronchemical properties. Applied Catalysis B: Environmental, 2018, 226: 234–241
20. Sha Z, Chan H S, Wu J. Ag_2CO_3/UiO-66(Zr) composite with enhanced visible-light promoted photocatalytic activity for dye degradation. Journal of Hazardous Materials, 2015, 299: 132–140
21. Cao J, Yang Z H, Xiong W P, Zhou Y Y, Peng Y R, Li X, Zhou C Y, Xu R, Zhang Y R. One-step synthesis of Co-doped UiO-66 nanoparticle with enhanced removal efficiency of tetracycline:

simultaneous adsorption and photocatalysis. Chemical Engineering Journal, 2018, 353: 126–137

22. Shen L, Luo M, Liu Y, Liang R, Jing F, Wu L. Noble-metal-free MoS_2 co-catalyst decorated UiO-66/CdS hybrids for efficient photocatalytic H_2 production. Applied Catalysis B: Environmental, 2015, 166: 445–453
23. Wu Y, Xu M, Chen X, Yang S, Wu H, Pan J, Xiong X. CTAB-assisted synthesis of novel ultrathin $MoSe_2$ nanosheets perpendicular to graphene for the adsorption and photodegradation of organic dyes under visible light. Nanoscale, 2016, 8(1): 440–450
24. Dai C, Qing E, Li Y, Zhou Z, Yang C, Tian X, Wang Y. Novel $MoSe_2$ hierarchical microspheres for applications in visible-light-driven advanced oxidation processes. Nanoscale, 2015, 7(47): 19970–19976
25. Ren Z, Liu X, Chu H, Yu H, Xu Y, Zheng W, Lei W, Chen P, Li J, Li C. Carbon quantum dots decorated $MoSe_2$ photocatalyst for Cr(VI) reduction in the UV–vis–NIR photon energy range. Journal of Colloid and Interface Science, 2017, 488: 190–195
26. Chu H, Liu X, Liu B, Zhu G, Lei W, Du H, Liu J, Li J, Li C, Sun C. Hexagonal 2H-$MoSe_2$ broad spectrum active photocatalyst for Cr(VI) reduction. Scientific Reports, 2016, 6(1): 35304
27. Wu M H, Lee J T, Chung Y J, Srinivaas M, Wu J M. Ultrahigh efficient degradation activity of single- and few-layered $MoSe_2$ nanoflowers in dark by piezo-catalyst effect. Nano Energy, 2017, 40: 369–375
28. Zhang Y, Gong Q, Li L, Yang H, Li Y, Wang Q. $MoSe_2$ porous microspheres comprising monolayer flakes with high electrocatalytic activity. Nano Research, 2015, 8(4): 1108–1115
29. Wang M, Peng Z, Qian J, Li H, Zhao Z, Fu X. Highly efficient solar-driven photocatalytic degradation on environmental pollutants over a novel C fibers@$MoSe_2$ nanoplates core–shell composite. Journal of Hazardous Materials, 2018, 347: 403–411
30. Cavka J H, Jakobsen S, Olsbye U, Guillou N, Lamberti C, Bordiga S, Lillerud K P. A new zirconium inorganic building brick forming metal organic frameworks with exceptional stability. Journal of the American Chemical Society, 2008, 130(42): 13850–13851
31. Wang Y, Zhao J, Chen Z, Zhang F, Guo W, Lin H, Qu F. Construction of Z-scheme $MoSe_2$/CdSe hollow nanostructure with enhanced full spectrum photocatalytic activity. Applied Catalysis B: Environmental, 2019, 244: 76–86
32. Dong W, Wang D, Wang H, Li M, Chen F, Jia F, Yang Q, Li X, Yuan X, Gong J, Li H, Ye J. Facile synthesis of In_2S_3/UiO-66 composite with enhanced adsorption performance and photocatalytic activity for the removal of tetracycline under visible light irradiation. Journal of Colloid and Interface Science, 2019, 535: 444–457
33. Yu Y, Nam G H, He Q, Wu X J, Zhang K, Yang Z, Chen J, Ma Q, Zhao M, Liu Z, Ran F R, Wang X, Li H, Huang X, Li B, Xiong Q, Zhang Q, Liu Z, Gu L, Du Y, Huang W, Zhang H. High phase-purity 1T′-MoS_2- and 1T′-$MoSe_2$-layered crystals. Nature Chemistry, 2018, 10(6): 638–643
34. Yi J, Li H, Gong Y, She X, Song Y, Xu Y, Deng J, Yuan S, Xu H, Li H. Phase and interlayer effect of transition metal dichalcogenide cocatalyst toward photocatalytic hydrogen evolution: the case of $MoSe_2$. Applied Catalysis B: Environmental, 2019, 243: 330–336
35. Qu Y, Medina H, Wang S W, Wang Y C, Chen C W, Su T Y, Manikandan A, Wang K, Shih Y C, Chang J W, Kuo H C, Lee C Y, Lu S Y, Shen G, Wang Z M, Chueh Y L. Wafer scale phase-engineered 1T-and 2H-$MoSe_2$/Mo core-shell 3D-hierarchical nanostructures toward efficient electrocatalytic hydrogen evolution reaction. Advanced Materials, 2016, 28(44): 9831–9838
36. Gopalakrishnan D, Damien D, Shaijumon M M. MoS_2 quantum dot-interspersed exfoliated MoS_2 nanosheets. ACS Nano, 2014, 8(5): 5297–5303
37. Liu M, Li C, Zeng Q, Du X, Gao L, Li S, Zhai Y. Study on removal of elemental mercury over MoO_3-CeO_2/cylindrical activated coke in the presence of SO_2 by Hg-temperature-programmed desorption. Chemical Engineering Journal, 2019, 371: 666–678
38. Du C, Nie S, Zhang C, Wang T, Wang S, Zhang J, Yu C, Lu Z, Dong S, Feng J, Liu H, Sun J. Dual-functional Z-scheme CdSe/Se/BiOBr photocatalyst: generation of hydrogen peroxide and efficient degradation of ciprofloxacin. Journal of Colloid and Interface Science, 2022, 606(2): 1715–1728
39. Nie X, Wang J, Duan W, Zhao Z, Li L, Zhang Z. Effects of different crystallization methods on photocatalytic performance of TiO_2 nanotubes. Applied Physics A: Materials Science & Processing, 2021, 127(11): 879
40. Zhang N, Liu S, Fu X, Xu Y J. Fabrication of coenocytic Pd@CdS nanocomposite as a visible light photocatalyst for selective transformation under mild conditions. Journal of Materials Chemistry, 2012, 22(11): 5042–5052